distributions on a large-scale gas turbine blade under low speed conditions. Jin and Goldstein [15] used a naphthalene sublimation technique in accordance with the heat/mass transfer analogy to obtain heat transfer coefficients from measured mass transfer data. The effects of tip clearance, Reynolds number, and turbulence intensity were investigated on a flat tip rotor blade. Recently, Krishnababu et al. [16] carried out a numerical investigation to study the flow and heat transfer in the tip region. Their numerical code was validated using experimental data from Newton et al. [17] for low speed incompressible flow. Palafox et al [18],[19] made detailed over-tip flow and heat flux measurements in a "super scale" incompressible. Of course, all the above are for incompressible flow, and it is uncertain that they represent the transonic flow in a modern high-pressure turbine.

Of the few engine-scale transonic experiments performed which are published in the open literature, Polanka et al. [20] presented simultaneous pressure and heat transfer measurements for the turbine tip shroud region from a fully-rotating turbine stage. These measurements provided some of the details needed for accurately quantifying the true flow condition in the complex flow regime which exists near tips. Rotating turbine experiments were performed by Thorpe et al. [21], who investigated blade-tip heat transfer using heat flux gauges instrumented on the mean camber line of the blade tip in a transonic rotating turbine. The experimental condition was closely engine-representative and provides data at discrete locations on the blade tip. Dunn and Haldeman [22] presented heat-flux measurements for the tip region of a rotating blade with a recessed tip for a full-stage rotating turbine with transonic vane exit conditions. Heat transfer using heat flux gages on a rotating tip was studied by Molter et al. [23] for a high-pressure transonic turbine stage. They performed heat transfer and pressure measurements on a flat as well as a squealer tip and found that at the fundamental vane-crossing frequency, wake/shock disturbances can be significant on the tip surface. Tallman et al. [24] presented both heat transfer measurements and predictions for an airfoil at different locations (including endwalls and rotor tip) in a modern, 1 stage high-pressure, transonic turbine. Key and Arts [25] investigated the aerodynamic flow fields for flat and squealer types of transonic blade tips using oil flow visualizations and static pressure measurements. Investigations which consider the transonic nature of near-tip flows at engine-operating conditions were reported by Moore & Elward [26], Wheeler et al [27], and Zhang et al. [28]. These studies all indicate that shock waves form within the tip gap, creating large local pressure gradients which significantly affect local boundary-layer development. The combined experimental and CFD study of Zhang et al. [28] is the first to provide data on the presence of multiple and repeated heat transfer variations in the forms of stripes, which are present for the rear portion of a transonic tip surface. According to these investigators, these stripes are linked with a pattern of shock wave initiations and reflections.

The present study provides new information on the aero-thermal performance of a transonic turbine blade tip with different tip gap magnitudes. Both experimental and numerical results are given to enhance understanding of complex aero-thermal performance in the tip region at engine representative aerodynamic conditions, and to validate CFD modeling and predictive capabilities for a challenging problem of vital practical interest.

The present investigation is presented in two parts: Part I (the present paper) focuses on heat transfer on the tip and near-tip blade surfaces, while Part II examines aerodynamic loss. The present paper presents heat transfer data for a transonic blade tip with three tip gaps (g/S=0.5%, 1.0%, and 1.5%) for engine representative experimental conditions. Numerical predictions are conducted using the Rolls-Royce HYDRA suite for the same geometry and flow conditions. The CFD capability is assessed by the experimental results. As such, the numerical predictions give detailed flow structural characteristics which provide means for interpretation of experimentally measured surface Nusselt number distributions.

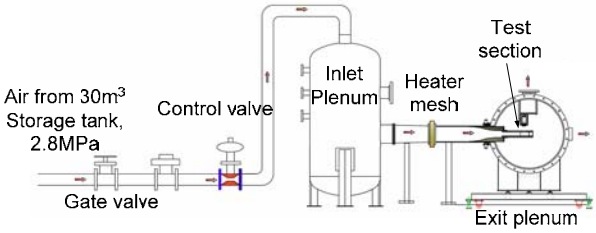

Figure 1 The schematic of the Oxford High Speed Linear Cascade research facility.

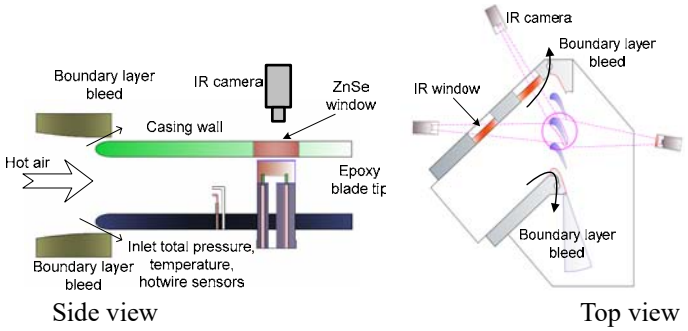

Figure 2 Schematic diagrams of the test section.

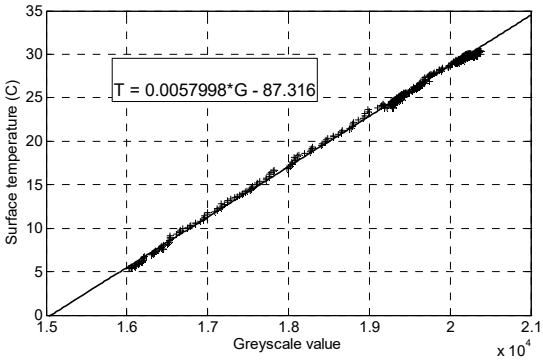

Figure 3 Infrared camera *in-situ* calibration data.

2 EXPERIMENTAL APPARATUS AND TECHNIQUES

The experiments are conducted in the Oxford University High-Speed Linear Cascade research facility, which is shown schematically in Fig. 1. The test section is mounted inside a pressurized plenum, which provides an environment wherein Mach number and Reynolds number can be varied independently. Figure 2 shows the details of the test section with 4 passages and 5 blades (including two sidewalls representing a suction side and a pressure side). The tip gap is adjustable for the middle three blades. Boundary layer bleeds are built on all four inlet duct walls, which ensure appropriate endwall and casing boundary layer condition. One movable tailboard is attached to the suction side sidewall. During the commissioning of the test rig, the boundary layer bleeds and tailboard are adjusted to achieve desired blade Mach number distribution as well as cascade periodic flow. To verify the flow periodicity, a three-hole probe is pitch-wise traversed one axial chord downstream of the test section. Note that no pressure side tailboard is present due to observations related to the flow periodicity and concerns regarding shock wave reflections.

A heater mesh element is installed upstream of the test section to provide a step increase in mainstream flow temperature [29]. During each blowdown test, 100 kW electrical power, operating at 100V, is dissipated in the heater mesh to abruptly raise the mainstream temperature by 25°C. As shown in Fig. 2, a zinc selenide window is placed on the top casing wall to provide optical access to the central test blade tip surface for a FLIR A325 Researcher infrared camera. This FLIR A325 camera is used to measure spatially-resolved surface temperature distributions, as it is equipped with a RJ-45 Gigabit Ethernet connection that supplies 16-bit 320x240 infrared images at a data acquisition rate of 60 Hz.

The blade tip surface is made of epoxy resin with very low thermal conductivity by Stereolithography technique (also known as 3-D printing). The gap between tip and casing is adjustable. Two thermocouples with wire diameter of 25 μm (0.001 inches) are placed on the tip surface to provide *in-situ* data for calibration of the infrared camera images. These fast-response thermocouples enable measurements of time-resolved surface temperatures.

The PID feedback control system, contained as part of the main flow pressure regulator for the wind tunnel, provides steady flow conditions at the inlet of the test section during every blowdown test. With this arrangement, a relatively constant total pressure of 200kpa (absolute) is maintained for approximately 90 seconds.

These steady flow conditions are verified from measurements obtained at the inlet of the test section, which are made with a pitot-static probe and a total temperature thermocouple, which are located one axial chord distance upstream of the blade leading edges. A total pressure rake is also used to check the inlet flow uniformity throughout the inlet. Hotwire surveys are also conducted one axial chord upstream of the test blade to measure the inlet turbulence and inlet casing wall boundary layer profile. Note that the profile is employed as the inlet casing wall boundary condition of the CFD study presented in the later part of this paper. Multiple pressure taps are placed on the blade midspan and 95 percent of the span (near tip) to measure surface static pressure values for determination of blade isentropic Mach number distributions. Mid-span isentropic Mach number profiles are reported by O'Dowd et al. [30], and contain a peak suction-side Mach number of approximately 1.2. Table 1 summarizes the flow conditions for the present study.

Table 1 Transonic flow conditions for the present study

Inlet Mach number	0.28
Inlet Reynolds number (based on C_x)	0.60×10^6
Mass flow rate	3.23 kg/s
Exit Mach number	1
Exit Reynolds Number(based on C_x)	1.27×10^6

A transient thermal measurement technique is employed in the present study to determine local heat transfer coefficients [30]. As previously indicated, an abrupt step-change in the mainstream temperature is achieved by employing a heater mesh installed upstream of the test section. During each blowdown test, the spatially-resolved temperature history for the tip surface is acquired using the infrared camera and recorded into a digital file. Surface temperature readings measured by the thermocouples located on the tip surface are recorded simultaneously. An example of in situ calibration data obtained with these devices and procedures is presented in Figure 3, which shows a linear relationship between grayscale values from the infrared camera and temperature readings from a surface thermocouple, obtained during a typical single blown-down run. Note that radiation reflection from other objects, surface emissivity variations, and zinc selenide window transmissivity are all rigorously accommodated by the in-situ infrared camera calibration process.

Because of the very low conductivity of the tip material, heat transfer on the blade tip surface is modeled using a semi-infinite solid conduction analysis procedure. A penetration depth analysis is performed to justify the selected duration of

the transient heat transfer. (within 5 seconds the depth which reaches 10% of the surface temperature is 1.4mm). With this approach, a complete heat flux history is reconstructed from temperature traces for each blade tip pixel location. The impulse data processing technique, developed by Oldfield [31], is then employed to reconstruct the heat flux from temperature-time traces. This method uses known pairs of exact solutions to obtain an impulse response filter to convert temperature into heat flux using Fast Fourier Transforms. Oldfield [31] describes this process as being much more sophisticated and efficient than other heat flux reconstruction approaches. This method is also described and employed by O'Dowd et al. [30].

Figure 4 shows an example of experimental data which are measured and determined using these techniques. Here, surface heat flux is presented as it varies with surface temperature for one blade tip pixel location. Note that a linear relationship between the heat flux and wall temperature is present. From these data, local blade tip heat transfer coefficients are determined, where heat transfer coefficient is defined using the equation given by

$$\dot{q} = h(T_{ad} - T_w) \qquad (1)$$

Within Fig. 4, the local heat transfer coefficient is given by the slope of the heat flux versus surface temperature data, and adiabatic wall temperature is determined by extrapolation of the data to the axis intercept which corresponds to zero heat flux. A similar reconstruction method is then used for each and every one of the 320x240 blade tip surface pixel locations.

The experimental uncertainties are determined using a combination of partial derivatives described by Kline and McClintock [33], a jitter analysis described by Moffat [34] and the standard error of estimate resulting from the errors created when determining the IR calibration curve, as described in Coleman and Steele [35]. The overall uncertainty for Nusselt number is 9.5%, and uncertainty for adiabatic wall temperature is 1.2K. Reproducibility of heat transfer results is determined from multiple test runs. The area-weighted average of the normalized standard deviation is less than 6%. A detailed uncertainty analysis and qualification of the current heat transfer measurement technique is presented by O'Dowd [26].

Note that the 1-D conduction assumption used in the present study is unlikely to be accurate around the perimeter regions of the blade tip surface. Thus higher uncertainties exist when the edges are approached.

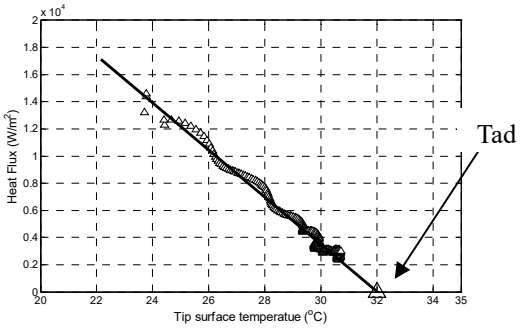

Figure 4. An example of heat flux versus temperature history for one location on the tip surface.

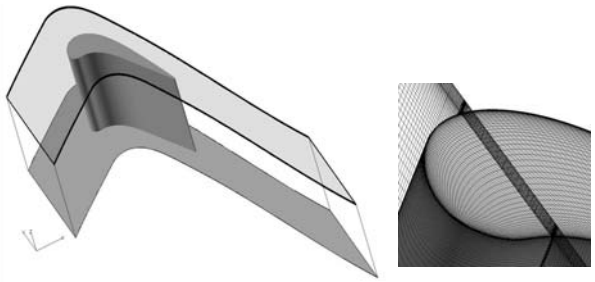

Figure 5. Computational domain and mesh employed in the present study.

3 COMPUTATIONAL APPROACH DETAILS

The Rolls-Royce HYDRA suite is employed in the present numerical predictions. The core of the software is a preconditioned Runge-Kutta solver of the discrete Euler or Reynolds-averaged Navier-Stokes equations (RANS). In this paper, steady RANS calculations are performed and the Spalart-Allmaras (SA) turbulence model is implemented. The computational domain consists of one blade with periodic boundary conditions. The blade definition, tip gap clearance, flow angle, and inlet boundary conditions are input such that they are exactly same as the experimental setup. The ICEM software is employed for mesh generation. Figure 5 presents the computational domain and mesh employed for the present study.

No "wall function" is employed in the present study. The mesh has a multi-block structure, with a total grid size of about 6 million cells. Near tip surface y^+ values are less than 5. Considering the large variation of the local flow structure, a large portion of the tip region has a y^+ of 1-2. An isothermal wall thermal boundary condition is employed on all the wall surfaces. All solutions presented are also grid-independent, which is verified by negligible changes to predicted quantities as the grid density (near wall grid size/expansion ratio) is changed. The tip surface heat flux values are not changed while further reducing near wall grid size.

Visualization of the Hydra solutions is accomplished using the commercial FieldView software package.

4 TIP HEAT TRANSFER RESULTS

Presented in this section are tip surface Nusselt number distributions obtained from experiments and HYDRA numerical predictions for three different tip gaps: 0.5, 1.0, and 1.5 percent, where each quantity is the ratio of tip gap to blade span. HYDRA predictions of Mach number and turbulence viscosity ratio distributions in the flow over and near the tip are also presented.

Nusselt number distributions

Figure 6 presents the spatially-resolved experimental data for Nusselt numbers with three tip gaps (g/S=0.5%, 1.0%, and 1.5%). For all three situations, the Nusselt number decreases as the tip gap is reduced for the most of the blade tip surface. For all tip gaps investigated, the Nusselt number is higher near the leading edge region of the tip surface, and relatively low on the middle and rear parts of the blade tip. A small "hot spot" is present which is located very near the trailing edge portion of the tip.

The Nusselt number contours from HYDRA predictions for the three tip gaps, which are shown in Fig. 7, are in close agreement with the experimental measurements. Notice that most all of the experimentally-measured surface Nusselt number variations on the tip surface are well-captured within the CFD predictions. This includes both overall variations as well as detailed local variations.

Circumferential-averaged Nusselt number variations along the axial chord are presented in Fig. 8. Overall, Fig. 8 indicates that the HYDRA code gives circumferential-averaged trends which are consistent with experimental results, even though differences between Nusselt number data from different tip gaps are under-predicted.

Of particular importance in both the prediction and experimental results are increased Nusselt number near pressure-side trailing edge region as the tip gap becomes smaller. (This is evident in Fig. 8, can also be observed in Figs 6 and 7.) This is believed to be due to changes to local turbulent transport with tip gap magnitude.

In the previous study for the 1.5% tip gap, Zhang et al. [28] reported that the multiple heat transfer stripes on tip surface (rear part of the tip) are present as a result of shock wave reflections (Figs. 6 and 7). The pattern of high and low heat transfer stripes, normal to the flow direction, are due to the rapid acceleration and deceleration which occur prior to and across the shock reflections on the tip, which thus dominate the turbulence production and dissipation. In the tip region with supersonic flow, the high heat flux is dominated by the enhanced turbulence thermal diffusion (which is often augmented under an adverse pressure gradient after a shock wave) rather than a wall shear stress (also see Fig. 10). The shock-boundary layer interaction contributes to further enhancement of heat transfer to the blade tip near the shock foot.

Mach number distributions

Predicted Mach number distributions, determined by local total and static pressures, are presented in Fig. 9 for the plane which is located in the middle of the tip gap. For all three tip gaps, the flow is subsonic within the leading edge region of the tip gap. Here, the local Mach number generally decreases as the tip gap magnitude becomes less. The same Mach number trend with tip gap is present farther downstream along the blades, at locations greater than 30 to 40 percent of the axial chord length, when the flow becomes supersonic.

Figure 10 shows Mach number contour for a cut plane on the blade tip surface along the leakage flow streamlines direction for a tip gap g/S=1.0%. The abrupt onset of the supersonic flow evidences the presence of shock waves within the tip gap. Additional abrupt Mach number changes at multiple locations farther downstream indicate shock wave reflections, especially for bigger tip gaps. These variations are consistent with shock wave reflection reported by Zhang et al. [28].

Note that Fig. 9 shows that the shock wave reflections are less evident for the 0.5 percent tip gap case. With this smaller tip gap, the Mach numbers within the supersonic flow region are somewhat less, and the resulting shock waves are also weaker.

Turbulent to laminar viscosity ratio (μ_T/μ_L) distributions

To provide additional understanding of measured and predicted surface Nusselt number distributions, Turbulent to laminar viscosity ratio (μ_T/μ_L) distributions just above the tip surface (within the boundary layer) are predicted. The spatially-resolved results for a tip gap g/S=1.0% are given in Fig. 11. From these data, two principal features are identifiable. (1) The region marked "A" is associated with the high turbulence stripe origins near the leading edge region, which extend across the tip surface. According to Zhang et al. [28], local streamlines for the tip leakage flow within this region change direction and travel toward the axial direction. The cross-flow diffusion which is present here then results in enhanced local turbulence production and enhanced local turbulent transport. These then result in enhanced local Nusselt numbers. (2) The region marked "B" is associated with enhanced turbulence transport in the vicinity of the local "hot-spot" which is located near the pressure-side trailing edge region.

Thus, local heat transfer augmentations on the transonic blade tip are closely correlated with enhanced turbulence thermal diffusion for both the frontal part of the tip surface, as well as for the trailing edge region.